Volume 17
Number 7
21 February 2021
Pages 1703–2012

Soft Matter

rsc.li/soft-matter-journal

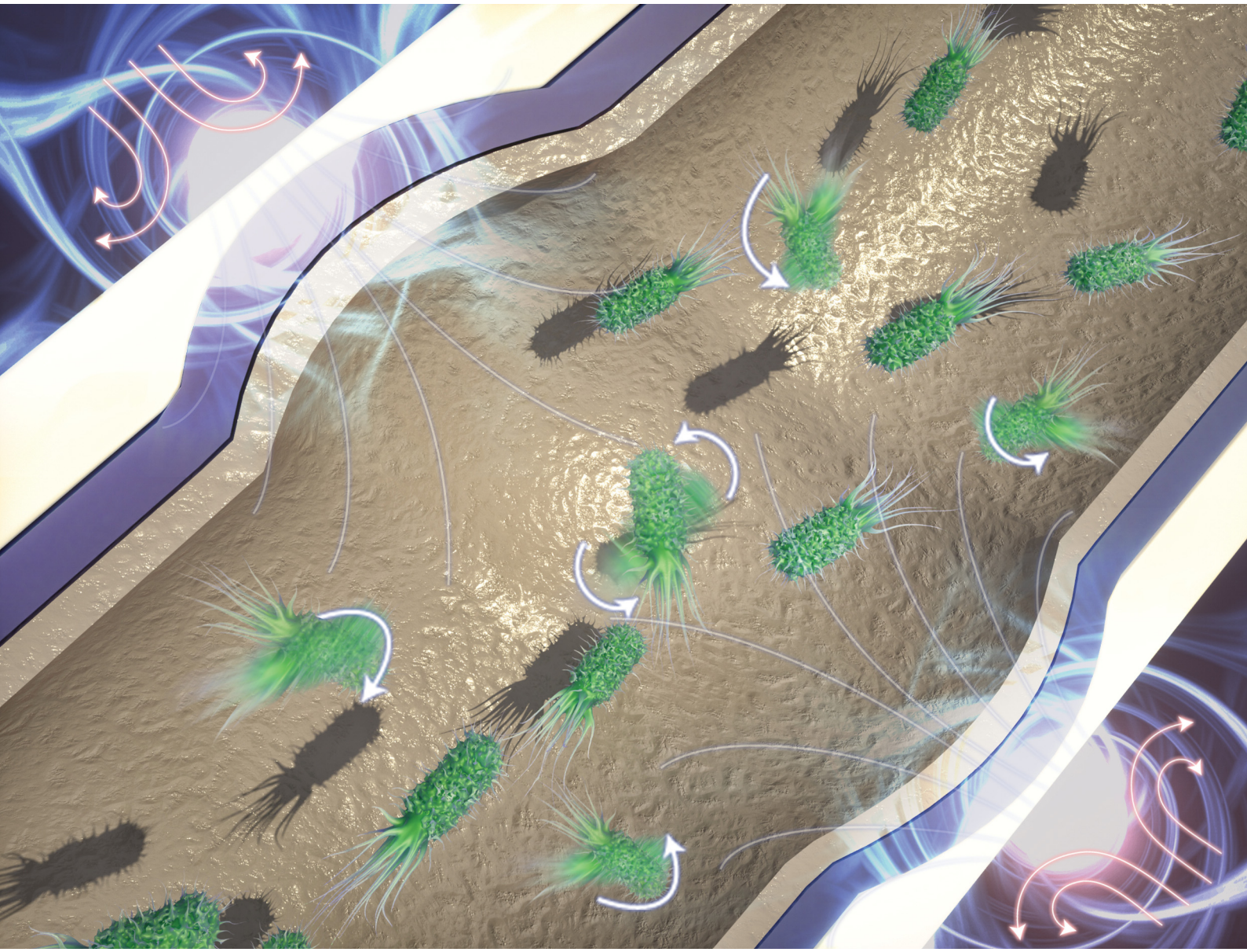

ISSN 1744-6848

ROYAL SOCIETY OF CHEMISTRY

PAPER
Jangho Kim, Hoon Eui Jeong *et al.*
Biofouling-resistant tubular fluidic devices with magneto-responsive dynamic walls

Published on 20 January 2021. Downloaded by Ulsan National Institute of Science & Technology (UNIST) on 3/7/2023 5:43:09 AM.

Soft Matter

PAPER

View Article Online
View Journal | View Issue

Check for updates

Cite this: *Soft Matter*, 2021, **17**, 1715

Biofouling-resistant tubular fluidic devices with magneto-responsive dynamic walls†

Geonjun Choi,[a] Hangil Ko,[a] Hyejin Jang,[a] Insol Hwang,[a] Minho Seong,[a] Kahyun Sun,[a] Hyun-Ha Park,[b] Tae-Eun Park,[c] Jangho Kim*[d] and Hoon Eui Jeong *[a]

Received 7th November 2020,
Accepted 19th January 2021

DOI: 10.1039/d0sm01979h

rsc.li/soft-matter-journal

Biofouling of tubular fluidic devices limits the stability, accuracy, and long-term uses of lab-on-a-chip systems. Healthcare-associated infection by biofilm formations on body-indwelling and extracorporeal tubular medical devices is also a major cause of mortality and morbidity in patients. Although diverse antifouling techniques have been developed to prevent bacterial contamination of fluidic devices based on antimicrobial materials or nanoscale architectures, they still have limitations in biocompatibility, long-term activity, and durability. In this study, a new conceptual tubular fluidic device model that can effectively suppress bacterial contamination based on dynamic surface motions without using bactericidal materials or nanostructures is proposed. The fluidic device is composed of a magneto-responsive multilayered composite. The composite tube can generate dynamic surface deformation with controlled geometries along its inner wall in response to a remote magnetic field. The magnetic field-derived surface wave induces the generation of vortices near the inner wall surface of the tube, enabling sweeping of bacterial cells from the surface. As a result, the dynamic composite tube could effectively prevent biofilm formation for an extended time of 14 days without surface modification with chemical substances or nanostructures.

Introduction

Biofouling of the inner walls of fluidic channels hinders the stable long-term cell culture in microfluidic cell culture devices and also limits accurate biological and chemical analysis in diverse lab-on-a-chip systems.[1,2] Also, biofilm formation on the surface of medical devices is a major cause of healthcare-associated infections (HAIs), leading to severe morbidity and mortality in patients.[3] Among several types of HAIs, more than 50% occur due to implanted medical fluidic devices such as urinary, vascular, and central line catheters, as well as respiratory ventilators.[4]

To prevent the biofouling of fluidic systems, diverse strategies have been developed; these include vibroacoustic stimulation,[5] surface coating with hydrogel[6] or a quorum sensing inhibitor,[7] and surface modification with bactericidal materials such as silver alloys,[8] nanoparticles,[9] and nitrous oxide.[10] However, many of these have limited biocompatibility and long-term stability which hinders their practical application.[11] Bioinspired nanostructures and polymeric materials have been developed *via* a biocompatible and sustainable antifouling strategy; these include a lotus leaf-inspired superhydrophobic surface,[12–14] insect wing-inspired nanostructure,[15–17] slippery liquid-infused surface (SLIPS),[18,19] and membrane-mimicking zwitterionic polymers.[20,21] Although these bioinspired approaches have demonstrated remarkable bio- and eco-friendly antifouling capabilities against various bacterial species, they have mostly focused on the static structures or material aspects of nature. The bioinspired micro/nano structures and materials can also be degraded, fractured, or

[a] *Department of Mechanical Engineering, Ulsan National Institute of Science and Technology, Ulsan 44919, Republic of Korea. E-mail: hoonejeong@unist.ac.kr*
[b] *Department of Mechanical Engineering, Wonkwang University, Jeonbuk 54538, Republic of Korea*
[c] *School of Life Science, Ulsan National Institute of Science and Technology, Ulsan 44919, Republic of Korea*
[d] *Department of Rural and Biosystems Engineering, Chonnam National University, Gwangju 61186, Republic of Korea. E-mail: rain2000@jnu.ac.kr*

† Electronic supplementary information (ESI) available: Fig. S1: Schematic of fabrication process of the composite tubular device with dynamic undulatory inner walls. Fig. S2: FEA of the fluid velocity field and magnitude of vorticity in the composite tube with dynamic undulatory inner walls. Fig. S3: FEA of the magnitude of vorticity in the dynamic tubes with undulatory waves of different periodic times and amplitudes. Fig. S4: FEA results show that the vortex generated by the surface waves did not disturb the overall fluid flow through the catheter. Fig. S5: A schematic illustration describing the terms of amplitude (H) and periodic time (T) of the surface wave. Fig. S6: A photograph of the unfolded tube's innermost walls stained with crystal violet after the 14 days-exposure to *B. subtilis* culture. Movie S1: Real-time fluorescence video recording of undulatory inner walls of the composite tube generated by the translation of a permanent magnet. Movie S2: Real-time monochromic video recording of undulatory inner walls of the composite tube generated by the translation of a permanent magnet. Movie S3: Real-time fluorescence video recording of tracer particles inside the dynamically undulating composite tube in response to a translating magnetic field. See DOI: 10.1039/d0sm01979h

Published on 20 January 2021. Downloaded by Ulsan National Institute of Science & Technology (UNIST) on 3/7/2023 5:43:09 AM.

irreversibly fouled under long-term exposure to a fouling environment.

In contrast to the static nanostructures or materials, diverse living systems such as living cells,[22,23] blood vessels,[23] bronchiole tubes,[24,25] glands,[26] intestines,[27,28] plant xylem,[29] and marine organisms (*e.g.*, Batoidea, mollusks, seaweeds, mussels, and sharks)[30,31] are efficiently able to resist surface-fouling for a prolonged period of time based on their dynamic actuating motions without using toxic chemicals. Inspired by the remarkable antifouling properties of the dynamic natural materials, recent studies have demonstrated that repeated cyclic wrinkling and unwrinkling can induce delamination of a biofilm adhered to surfaces.[23,32,33] When the surface wrinkles, the adhered biofilm deforms conformally while the change in surface curvature induces a build-up of elastic energy. Beyond a certain curvature, the increase in elastic energy forces delamination of the adhered biofilm from the wrinkled surface.[34] In addition to the surface wrinkling, dynamically actuating cilia structures have also been used to mechanically remove adherent foulants from surfaces both in water and air.[35]

These results demonstrated that dynamically actuating materials have a strong potential as a new active and efficient antifouling strategy for biomedical fluidic devices. However, despite the potential, studies on fouling-resistant fluidic devices with dynamic surfaces are still in their infancy and require further exploration. In addition, the antifouling mechanisms of the previous dynamic materials are mostly based on the removal of the already-established biofilms rather than the prevention of the initial bacterial attachment.[36,37] Because mature biofilms are highly difficult to remove,[38] fluidic devices that can fundamentally prevent initial bacterial adhesion could lead to the development of a more safe and efficient pathway towards the development of advanced fluidic and medical devices.[39,40]

In this study, a new biofouling-resistant tubular fluidic device model that can fundamentally inhibit bacterial adhesion based on its dynamic undulatory surface motions is proposed. The proposed device is composed of magneto-responsive multiple layers that can generate coordinated dynamic sinusoidal surface waves along its inner wall. The dynamic undulatory inner wall motions of the device generate vortices near the inner surface of the device and therefore, fundamentally prevent bacterial adhesion on its surface. Up to 99.8% reduction in the formation of biofilm was observed on the surface of the dynamic tube compared to that of the static control device, despite being exposed to the bacterial culture for 14 days. Our findings provide important implications and principles wherein fluidic devices with dynamic undulatory surfaces can significantly reduce bacterial contaminations of diverse lab-on-a-chip devices and indwelling and extracorporeal medical devices. Beyond the magnetic field-based active undulation mechanism, passive approaches that can generate dynamic surface motion by environmental forces or internal body forces can be harnessed for the development of advanced fluidic devices and implants based on the proposed principle.

Experimental

Fabrication of the composite tubular device with undulatory inner walls

The multilayered tube was fabricated sequentially starting from the inside to the outside (see Fig. S1 for the detailed fabrication procedure, ESI†). First, soft polyurethane acrylate (s-PUA) (Minuta Technology, Republic of Korea) containing a prepolymer (aliphatic urethane triacrylate oligomer) and a photoinitiator (Irgacure 184, 1-hydroxy-cyclohexyl-phenyl-ketone) was injected into a mold with a cylindrical hole with a diameter of 6.2 mm.[41] A cylinder core bar with a diameter of 6 mm was placed through the centerline of the cylindrical hole. The injected s-PUA was cured by a 10 min-ultraviolet (UV) exposure (λ = 250–400 nm, dose = 300 mJ cm^{-2}), after which the core bar coated with the cured s-PUA layer was placed into a second mold which had a larger cylindrical hole of a 10 mm diameter. A polydimethylsiloxane (PDMS) and carbonyl iron (CI) particle mixture solution was then drop-casted into the 2nd mold. The mixture consisted of a PDMS prepolymer (Sylgard 184, Dow Corning Korea, Republic of Korea), PDMS curing agent, and CI particles (diameter: 1–5 μm, C3518, Sigma Aldrich Korea, Republic of Korea) with a 100 : 1.5 : 150 weight ratio. Thermal curing of the mixture at 70 °C for 2 h resulted in a uniform coating of the active magneto-responsive layer (AML) around the s-PUA layer. After removing the core bar coated with the s-PUA layer and AML, it was placed into a third mold with a cylindrical hole with a diameter of 11.4–14.2 mm. A mixture of PDMS prepolymer-curing agent-silicone oil (O02-543-666, LK Lab Korea, Republic of Korea), with a 50 : 1 : 10 weight ratio, was poured into the 3rd mold and baked at 70 °C for 2 h to produce the resilient damping layer (RDL) around the AML. After curing the RDL, the cured sample was released from the 3rd mold, followed by the removal of the core bar from the sample. Finally, the sample was uniformly coated with a polyethylene terephthalate (PET) supporting layer (thickness: ~250 μm, Changsung, Republic of Korea), which resulted in a multilayered composite tube.

Control and visualization of the undulatory inner wall motions of the tubular device

For the circular arrangement of the magnetic field around the tube, 10 rectangular neodymium magnets (size: 10 mm in width × 5 mm in height × 10 mm in depth, magnetic flux density: 0.5 T, JL Magnet, Republic of Korea) were inserted and fixed in a 3D printed magnet holder. This holder was connected to a linear actuator (MightyZAP, iRROBOT, Republic of Korea), whose maximum speed and stroke length were 25 mm s^{-1} and 30 mm, respectively. Upon a translation of the magnet, undulatory surface waves were generated along the inner wall of the tube. The fabricated tube was cut in the longitudinal direction for the visualization of the undulatory motion in a cross-sectional view. Then, the dynamic motions were observed with a stereo zoom microscope (Axio Zoom V16, Zeiss, Germany). To obtain fluorescence images of the surface motion, rhodamine B (87180-1510, Junsei, Japan) was added to the s-PUA solution of the innermost wall layer.

 This journal is © The Royal Society of Chemistry 2021

Published on 20 January 2021. Downloaded by Ulsan National Institute of Science & Technology (UNIST) on 3/7/2023 5:43:09 AM.

Particle image velocimetry (PIV)

For real-time optical imaging of the fluidic behavior inside the device with dynamic walls, a PIV experiment was conducted. Fluorescence tracer particles (PMMA-Rhodamine B-particle, microParticles GmbH, Germany) (diameter: 20–50 μm, density: 1.19 g mL^{-1}) were added into the working fluid (NaCl solution, density: 1.19 g mL^{-1}). To generate dynamic motion of the inside walls, circular arranged magnets were linearly actuated in the longitudinal direction with the reciprocating speed of 20 mm s^{-1}. Traces of particles were then monitored using a stereo zoom microscope (Axio Zoom V16, Zeiss, Germany) and recorded with a microscope-mounted camera (iXon EMCCD, Andor Technology-Oxford Instruments, England). The trajectories and the velocity information of particles were analyzed and extracted using a particle tracking software (Imaris, Bitplane, Switzerland).

Anti-biofouling assay

In order to analyze the fouling-resistance of the composite tube, *Escherichia coli* (*E. coli*) (ATCC25404, ATCC, USA) was used as a model foulant. For preparation, *E. coli* was cultured in 5 mL of Luria broth (LB Broth Miller, BD Difco, USA) with a shaking incubator (VS-8480, Vision Scientific, Republic of Korea) overnight at 200 rpm and 37 °C until optical density measurement at 600 nm (OD_{600}) reached 0.1. After sterilizing the tube with 70% ethanol and a 1 min-UV exposure, the prepared bacterial suspension was loaded into the composite tube and incubated at 37 °C for controlled time intervals. During the incubation, the undulation of the inner wall of the tube was controlled using the circular-arranged magnets fixed on the linear actuator. After the incubation, the innermost wall layer was separated from the tube, and then washed with phosphate-buffered saline (PBS). To evaluate bacterial viability, the specimens were stained with fluorescent labeling reagents (BacLight™, L7012, Invitrogen, USA). The stained samples were kept at room temperature for 15 min in a dark environment and rinsed three times with PBS solution. Then, the sample was examined with a multiphoton confocal microscope (LSM 780 Configuration 16 NLO, Zeiss, Germany) and the areal coverage of the stained bacteria was analyzed using ImageJ software (NIH, Bethesda, MD, USA). For the colony-forming unit (CFU) analysis, the PBS-washed samples were transferred to falcon tubes with 1 mL of PBS, followed by vortexing for 5 min. Subsequently, serially diluted bacterial solutions were plated on LB agar, followed by an 18 h incubation. The grown bacteria were then counted to quantify the CFUs.

Crystal violet staining assay

For the crystal violet (CV) staining assay, the bacterial suspension was incubated inside the composite tube for 14 days (336 h) with and without surface undulations (T = 3 s, H = 0.63 mm) using the circularly arranged permanent magnets (here, T represents the periodic time for the reciprocating motion of the surface wave and H represents the amplitude of the surface wave, see Fig. S5, ESI†). After the incubation, the tubular device was cut and unfolded, which was followed by rinsing with PBS solution twice. The washed tube samples were then submerged in CV solution for 10 min, followed by washing with deionized (DI) water. The samples were incubated with 95% ethanol for 15 min. The ethanol was then mixed and diluted 2 times into a volume of 200 μL in a single well of a 96-well culture plate. Absorbance of each well was evaluated at 590 nm using a spectrophotometer (SpectraMax Plus 384, Molecular Devices, USA). The CV test was performed for three individual samples and the average values were obtained from the tests.

Finite element analysis (FEA)

For the analysis of interactions between the magnetic field, deformation of the tube, and the fluidic behavior inside the tube, FEA was carried out using multiphysics analysis (Comsol Multiphysics 5.3a, Comsol Inc., Sweden). Over 3 300 000 free tetrahedral elements were used for the numerical analysis.

Statistical analysis

Mann–Whitney's U test was conducted to compare two different conditions, and Kruskal–Wallis' H test was performed to compare

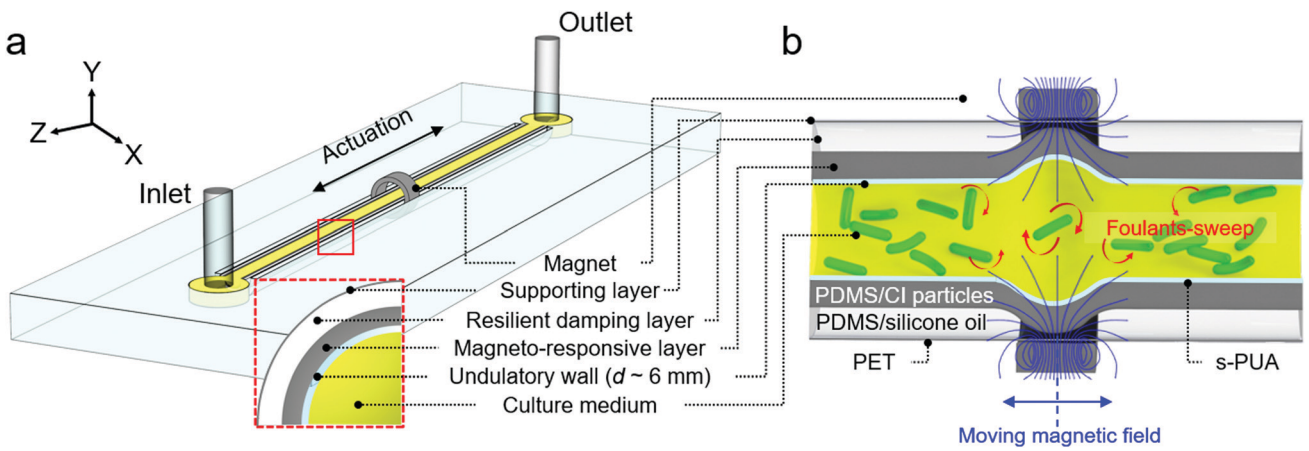

Fig. 1 Design of the composite tubular fluidic device with undulatory inner walls. (a) Tilted and (b) cross-sectional schematic illustrations showing the concept and structure of the dynamic composite-based tube with enhanced antifouling performance.

Published on 20 January 2021. Downloaded by Ulsan National Institute of Science & Technology (UNIST) on 3/7/2023 5:43:09 AM.

three or more conditions. Values of $p < 0.05$ were considered statistically significant.

Results and discussion

The structure of the fluidic device consisted of four layers: the innermost wall, an AML, a RDL, and the outermost supporting layer (Fig. 1a and b). The innermost wall layer was made of s-PUA with a thickness of 100 μm. The AML was made of a composite of PDMS and CI microparticles (diameter: 1–5 μm). This layer enables immediate local deformations of the tubular wall in response to the external magnetic field, without complicated wired connections (Fig. 1a and b). The RDL was composed of PDMS and silicone oil. The elastic modulus of this layer was optimized to ~10 kPa to enable depth-wise deformations of the innermost layer and AML without the outward protrusion of the damping layer (RDL). The outermost supporting layer was made of the PET film. This layer passivates the entire multilayered tubular structure of the device.

When a circular magnet moves along the lengthwise direction of the tube, the depth-wise deformation of the AML and the innermost layer propagates with the magnet (Fig. 1a and b), which results in the sinusoidal undulatory motions of the inner wall of the device. These dynamic undulatory surface waves were expected to prevent a close approach of foulants to the surface by generating local or global vortices near the inner surface of the device, and thus enable efficient suppression of biofilm formation in the tube (Fig. 1b). Experimental results described in the following sections were conducted in the setup described above.

Fig. 2a shows the deformations of the composite tube wall in response to an external magnetic field (see Movies S1 and S2, ESI†). To better investigate the dynamic deformation of the device, the innermost s-PUA layer was stained with rhodamine B (Fig. 2a-ii and b). Initially, the device had uniform inner wall geometry along its length direction without any deformation (Fig. 2b-i). When a magnet approached the device, the local inner wall region of the tube, which was close to the magnet, was deformed in the radial direction with an increased inner diameter of the tube, by the external magnetic field (Fig. 2b-ii). This deformation was generated by the AML composite containing the field-responsive CI particles. During the deformation, the RDL allows the radial deformation of the inner wall of the tube based on its low elastic modulus without the protrusion of the outer

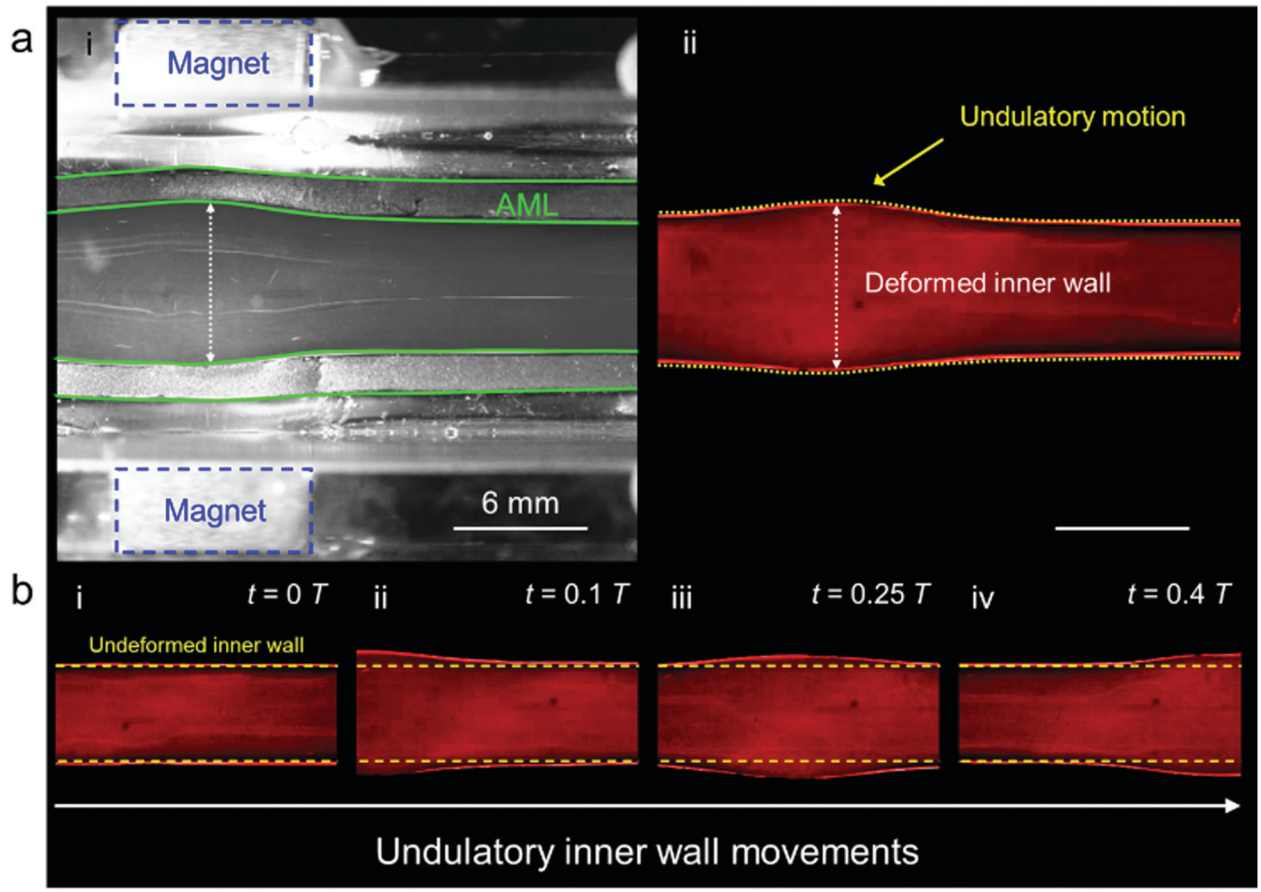

Fig. 2 Undulatory surface waves generated along the inner wall of the tubular fluidic device. (a) (i) Monochromic and (ii) fluorescence cross-sectional images of the undulatory inner wall motions of the tube in response to the magnetic field. (b) Time-lapse fluorescence images of the undulatory inner wall motions of the tube induced by the translation of a magnet (T = 3 s) at different times of (i) t = 0 T, (ii) 0.1 T, (iii) 0.25 T, and (iv) 0.4 T. Here, T represents the periodic time for the reciprocating motion of the wave. The innermost s-PUA layer of the tube was stained with rhodamine B.

 This journal is © The Royal Society of Chemistry 2021

Published on 20 January 2021. Downloaded by Ulsan National Institute of Science & Technology (UNIST) on 3/7/2023 5:43:09 AM.

surface of the tube. Upon the lengthwise movement of the magnet, the local circular deformation of the inner wall propagates in the longitudinal direction, resulting in sinusoidal topographical waves (Fig. 2b-iii and iv) (Movies S1 and S2, ESI†). During the propagation, the elastic RDL enables full restoration of the deformation.

The amplitude (H) and periodic time (T) of the surface wave are important factors that can affect the antifouling performance of the composite tube. T is the periodic time for the reciprocating motion of the surface wave (Fig. S5, ESI†), which can be adjusted by modulating the actuating speed of the magnetic field. For a fixed magnetic field and mechanical property (*i.e.*, elastic modulus) of each tubular layer, the depth (amplitude, H) of the deformation could be readily controlled by modulating the thickness of the RDL. Based on our theoretical analysis (Fig. 3), a thicker RDL resulted in a greater dimple depth in the inner wall. The deformation depth (δ) is determined by the compressive stiffness (k) of the RDL. The k and δ of the RDL can be determined by

$$k = \frac{(A \cdot E)}{t_{\mathrm{RDL}}} \quad (1)$$

$$\delta = \frac{(\sigma \cdot A)}{k} = \frac{(\sigma \cdot t_{\mathrm{RDL}})}{E} \quad (2)$$

where A and E are the area and elastic modulus of the RDL. These equations imply that thicker RDL results in lower compressive stiffness k and thus induce larger deformations δ under the same external stress.[42] In addition, a thicker RDL provides more underlying spaces deformable to the inner AML. For example, tubular devices with three different thicknesses of the RDL (t_{RDL} = 2.1 mm, 1.4 mm, and 0.7 mm) resulted in radial deformations (ΔR) of 0.63 mm, 0.51 mm, and 0.30 mm, respectively, under an identical field density (Fig. 3).

The dynamic inner wall motions of the tube can induce alterations in the fluid behavior inside the device. To investigate the fluidic behavior inside the tube, we performed PIV measurements of flow inside the tube. For the measurements, NaCl solution containing microparticles (diameter: 20–50 μm) was supplied into the tube. The NaCl solution was kept stationary without flowing in a specific direction and the dimple depth was maintained at 0.63 mm (H = 0.63 mm). Then, a magnet was reciprocated along the lengthwise direction (z-direction) with a periodic time of T = 3 s (speed of 20 mm s^{-1}) (Fig. 4a).

The PIV measurement results showed that the dynamic surface waves of the tube generated a noticeable vortex near the inner wall surface of the device (Fig. 4b and Movie S3, ESI†). Initially (t = 0 T), the fluid inside the tube was at rest across the device. When a dimple was generated by the magnet, outward fluid flow was generated by the newly generated dimple (t = 0.1 T). When the magnet was placed at the next position, the previously generated dimple was restored into the original un-deformed state while another outward fluid flow was generated on the newly generated

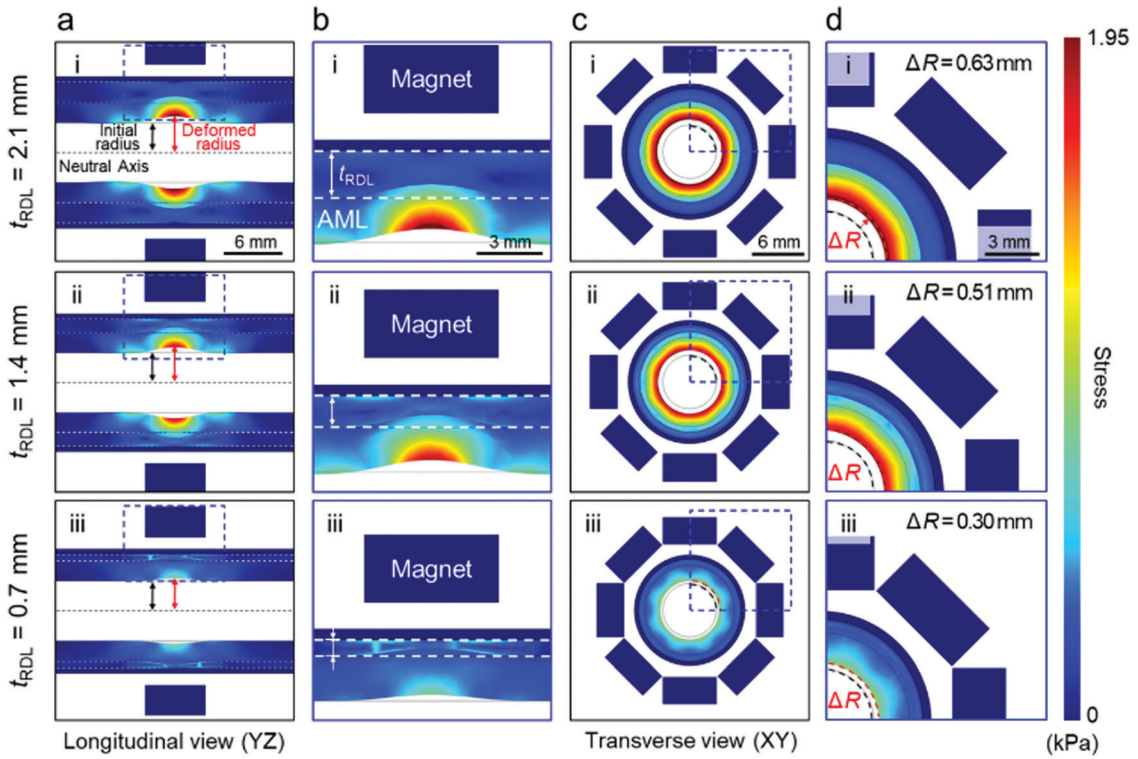

Fig. 3 Finite element analysis (FEA) of the deformation behavior of the composite tube under magnetic field. (a) Longitudinal views showing the simulated deformation behaviors of the tube with different thicknesses of RDL (i: 2.1 mm, ii: 1.4 mm, iii: 0.7 mm) and (b) their enlarged views. (c) Cross-sectional views showing the simulated deformation behaviors of the multilayered tube with different thicknesses of the RDL (i: 2.1 mm, ii: 1.4 mm, iii: 0.7 mm) and (d) their enlarged views.

Published on 20 January 2021. Downloaded by Ulsan National Institute of Science & Technology (UNIST) on 3/7/2023 5:43:09 AM.

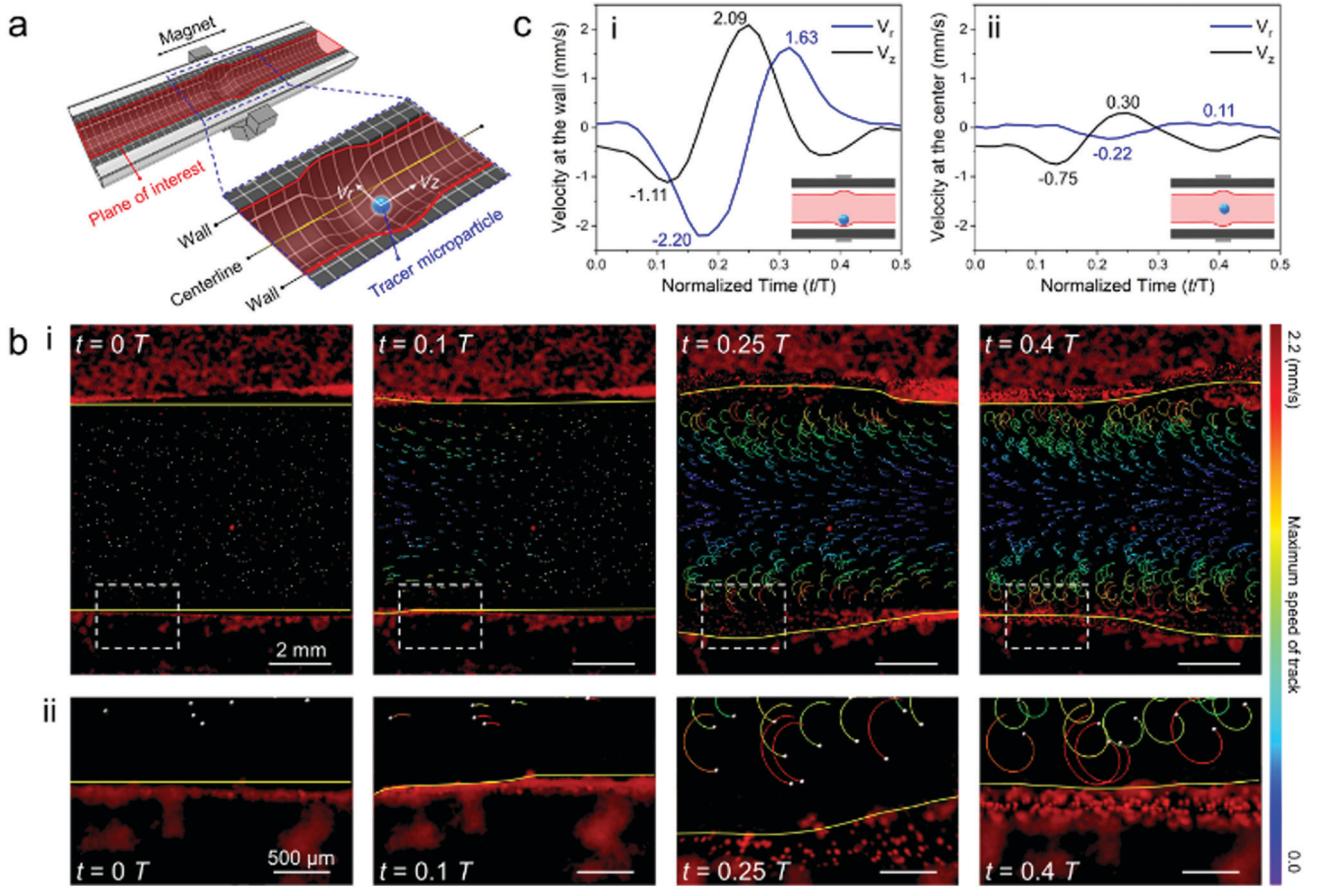

Fig. 4 Experimental analysis of the fluidic behavior inside the composite tube with dynamic walls (H = 0.63 mm, T = 3 s). (a) A schematic diagram of the experimental set-up and the planes of interest for the particle image velocimetry (PIV) experiment. (b) (i) Time-lapse fluorescence images showing the trajectories of tracer particles inside the tube with dynamic walls and (ii) their enlarged views. Colors of the trajectory lines indicate speed of each particle. (c) Velocity components of the flow in the radial (V_r), and longitudinal (V_z) directions at (i) the wall (r = 2.5, z = 0) and (ii) center (r = 0, z = 0) of the dynamic tube.

dimple (t = 0.25 T). Accordingly, this sequential dimple propagation resulted in the generation of a vortex along the inner surface of the tube (t = 0.4 T). Fig. 4c shows the particle velocity in the radial (V_r) and longitudinal (V_z) directions at the wall (r = 2.5, z = 0, Fig. 4c-i) and center (r = 0, z = 0, Fig. 4c-ii) of the tube during the propagation of the dimple. The particle near the dynamic wall exhibited remarkable changes in both, the magnitude and direction (Fig. 4c-i), while the particle at the center of the tube showed nearly zero velocity with minimal variations (Fig. 4c-ii). This result indicates that foulant particles near the dynamic tube wall would be engulfed in strong vortices and thereby cannot be easily attached onto the device wall.

To further investigate the fluidic behaviors inside the dynamic tube, numerical analyses were conducted using FEA. Governing equations of the fluidic behavior inside the device model were defined by the dynamic and kinematic coupling of stress tensors at the interface of fluid and solid domains.[43] Each end of the internal channel is set as an open boundary. The FEA confirmed that the dynamic surface waves of the tube resulted in significant changes in the velocity field of the fluid (Fig. S2a, ESI†) and vortex generation (Fig. S2b, ESI†) on the dynamic inner wall surface, which were overall in sufficient agreement with the experimental observations. The FEA further showed that surface waves with higher amplitudes H and lower periodic times T resulted in higher vorticity (Fig. S3, ESI†). Note that the vortex generated by the surface waves did not disturb the overall fluid flow through the tube (Fig. S4, ESI†).

To investigate the fouling-resistant properties of the tube with undulatory surfaces, *E. coli* cells were cultured on the dynamic s-PUA surfaces with undulatory waves of different periodic times (T = 3, 20, 60 s) and amplitudes (H = 0.30, 0.51, and 0.63 mm) for 18 h. *E. coli* cells were also cultured on a static surface as a control ($T = \infty$). Highly dense *E. coli* cells were observed on the static tubular surface, as indicated by the green color of the confocal microscopy image (Fig. 5a-I, i).

When the device surface underwent a dynamic undulatory motion, the number of adhered bacterial cells was noticeably lower than that on the static surface (Fig. 5a-I, ii–vi). The surface fouling was significantly reduced as the periodic time (T) of the surface wave decreased from 60 s to 3 s for a fixed amplitude (H = 0.63 mm) of the wave (Fig. 5a-I, ii–iv). According to the areal coverage (AC) analysis, the tube with dynamic walls of T = 60, 20, and 3 s (H = 0.63 mm) exhibited 43.3, 85.4, and 93.2% lower AC values, respectively, than those of the tube with

 This journal is © The Royal Society of Chemistry 2021

Published on 20 January 2021. Downloaded by Ulsan National Institute of Science & Technology (UNIST) on 3/7/2023 5:43:09 AM.

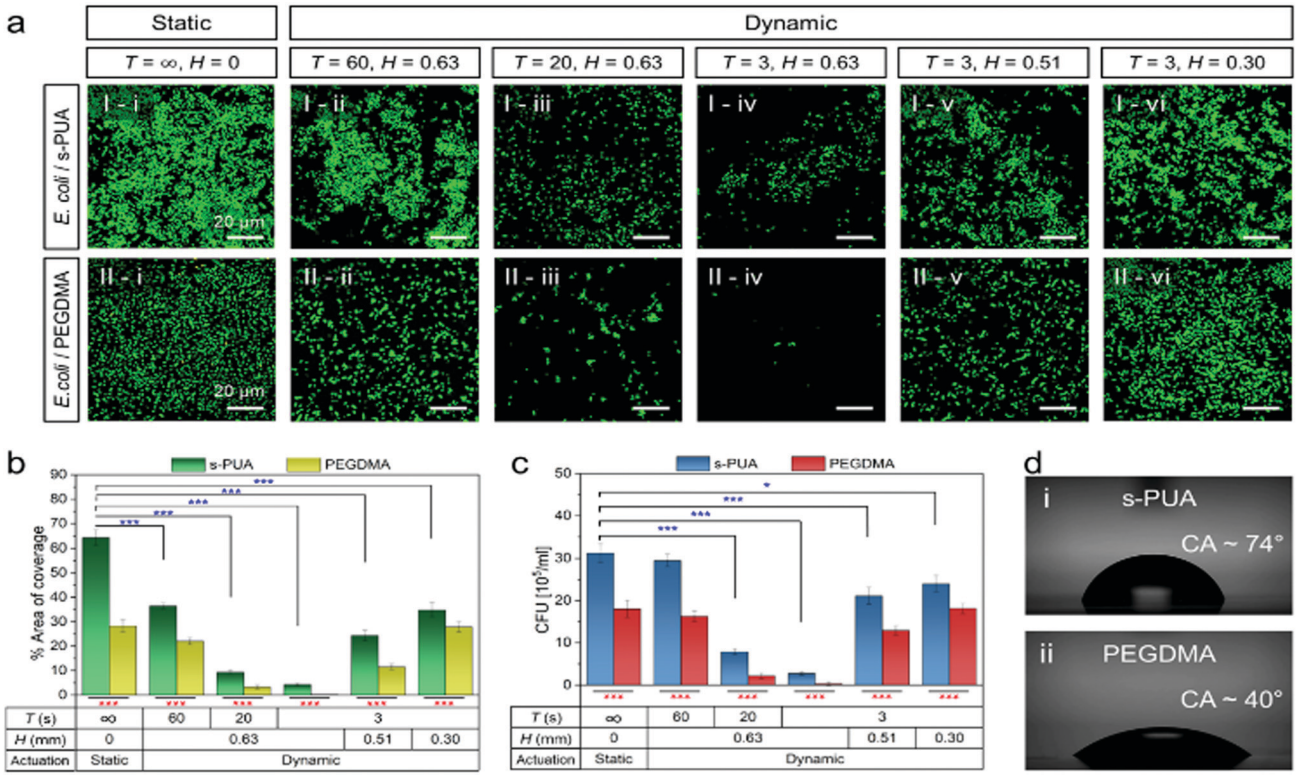

Fig. 5 Antifouling properties of the tube with a dynamic inner wall. (a) Confocal microscopy images of the *E. coli* cultured (18 h at 37 °C) inside the tubes with the s-PUA (top-row) and PEGDMA (bottom-row) innermost layers under different undulating conditions (T and H). (b) Areal coverages and (c) CFU of the live *E. coli* cultured in the different static and dynamic tubes. The data were analyzed using Mann–Whitney U test (red) or Kruskal–Wallis' H test (blue) (n = 5, * $p < 0.05$, *** $p < 0.001$). (d) Contact angle of water droplets on the (i) s-PUA and (ii) PEGDMA surfaces.

static walls (Fig. 5b). This is because a faster surface undulation (lower T) resulted in more severe shear stresses and vortex, thus inhibiting a close access and attachment of planktonic bacteria to the device surface, as demonstrated in our PIV analysis (Fig. 4).[44] The amplitude of the wave also affected the antifouling performance of the tube. For a fixed periodic time of T = 3 s, the tube wall with a higher amplitude led to a higher fouling resistance (Fig. 5a-I, iv–vi). The tube with an H value of 0.63 mm exhibited 82.2% and 87.5% lower AC values than those of the tube with an H of 0.51 mm and 0.30 mm, respectively (Fig. 5b). The CFU analysis also showed an overall similar tendency with the AC analysis results (Fig. 5c).

To further enhance the antifouling performance of the tube with a dynamic undulatory wall, the innermost wall layer of the tube was prepared using poly(ethylene glycol) dimethacrylate (PEGDMA), instead of s-PUA. PEGDMA is a biocompatible hydrogel having an intrinsic antifouling property.[45–47] It can form a hydration layer on its surface based on its hydrophilic nature (Fig. 5d) which prevents a surface attachment of foulants including bacterial cells.[48–50] Furthermore, it is an UV-curable material which facilitates rapid surface coating and modification.[51–53] As expected, the tubular devices with a PEGDMA innermost wall showed enhanced antifouling performance compared to the counterpart samples made of s-PUA (Fig. 5a-II). For example, for the static sample, the PEGDMA-based tube showed a 56.0% lower AC value compared to that of the s-PUA based tube. Furthermore, the PEGDMA-based tube with a surface undulation of T = 3 s and H = 0.63 mm exhibited a 95.9% lower AC value compared to the s-PUA-based tube with the same surface undulation (T = 3 s, H = 0.63 mm). However, note that the surface undulation of the device resulted in antifouling performance superior to the surface coating of the tube with an intrinsically antifouling PEGDMA. For example, the tube with an undulating s-PUA inner wall with a T value of 3 s and H value of 0.63 mm showed 84.6% lower AC than that of the tube with a static PEGDMA inner wall (Fig. 5b). Moreover, the reduction rates in the AC reached 93.2% and 99.8% for each tubular device with a s-PUA and PEGDMA inner wall, respectively, under a properly dynamic undulating condition (T = 3 s, H = 0.63 mm) compared to that of the s-PUA-based static tube. In contrast to the dynamic case, the reduction rate in the AC of the static PEGDMA-based tube was only 56.0% compared to that of the s-PUA-based static tube. These results demonstrate that the surface undulatory motions could provide a high-performance antifouling pathway for biomedical devices including a catheter towards an efficient and safe prevention of HAIs and CAIs, even without using surface coatings with bactericidal materials.

To further characterize the long-term antifouling performance of the dynamic tube, *E. coli* was cultured in the prepared model tube for 14 days with and without the surface undulation (T = 3 s, H = 0.63 mm) (Fig. 6). Fig. 6a shows the unfolded tubes

Published on 20 January 2021. Downloaded by Ulsan National Institute of Science & Technology (UNIST) on 3/7/2023 5:43:09 AM.

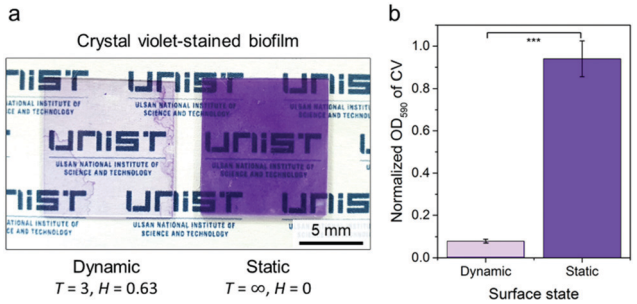

Fig. 6 Long-term antifouling tests of the tubular device with dynamic inner wall motions. (a) A photograph of the unfolded tube's innermost walls stained with crystal violet after the 14 days-exposure to *E. coli* culture with- (left) and without- (right) topographical wave generation (T = 3 s, H = 0.63 mm). (b) Normalized OD_{590} values of the CV-stained static and dynamic tubes (n = 10, *** $p < 0.001$ compared to static; the data were analyzed using Mann–Whitney U test).

stained with CV after a 14 days-exposure to the *E. coli* culture. As a result, the tube with continuous undulatory waves exhibits significantly lower CV staining compared to those without undulatory waves. The quantitative CV assay showed that the tube with dynamic undulation has a notable biofilm-resistance compared to the static tube (91.4% lower normalized OD_{590} compared to the static surface) (Fig. 6b). Note that our device also showed noticeable antifouling performance for Gram-positive bacteria *Bacillus subtilis* (Fig. S6, ESI†).

Conclusions

In summary, a new design of the tubular fluidic device model that consists of magnetic field-responsive multilayered composites for the effective suppression of biofouling of the tubular device was proposed. The field-responsive inner walls of the device could be dynamically undulated in a simple and controlled fashion with the external magnetic field. The PIV tests showed that the dynamic inner wall motions of the device can induce high vortices and shear stresses on the near surface of the device, fundamentally inhibiting the access of planktonic bacteria to the device surface. As a result, the dynamic tubular device exhibited considerable resistance against biofilm formation despite 14 days of exposure to bacterial cells. According to previous studies, shear stress alone cannot properly prevent biofilm formation on surfaces.[54,55] Local and global vortices combined with high shear flow generated on the undulatory surface of our device were highly effective to suppress surface fouling.

In this study, an external magnetic field was utilized to derive surface undulation of the device. While this approach enables active control over the surface motions, it requires an application of external magnetic field. Thus, it would be difficult to directly apply the proposed dynamic tube model to body-indwelling medical implants, while the dynamic tube model can be directly utilized in the development of fouling-resistant LOC systems. Beyond the magnetic field-based active undulation mechanism, passive approaches that can generate dynamic surface movement by external energy or internal body energy can be harnessed to develop dynamic surfaces-based antifouling fluidic systems. Significantly soft materials, rationally-designed micro/nanoscale structures, or a combination thereof could be possible solutions for achieving the passive undulatory mechanisms in biomedical fluidic devices. Nonetheless, the dynamic undulatory topography-based antifouling strategy proposed in this study could contribute to the development of biofouling-free LOC and medical devices by combining antifouling materials and nanostructures.

Author contributions

GC and HK equally contributed to this work. GC, HK, and HEJ designed the research. GC and HK prepared the samples and performed the experiments. GC, HJ, KS, and HHP performed the anti-biofouling assay. GC, IH, and MS performed the numerical analyses. GC, TEP, JK, and HEJ analyzed experimental and simulation results. GC, JK, and HEJ wrote the manuscript. All authors contributed to discussing the results and preparing the manuscript.

Conflicts of interest

There are no conflicts to declare.

Acknowledgements

This work was supported by the National Research Foundation of Korea (NRF) (2019M3C1B7025092) and Korea Electric Power Corporation (R19XO01-26).

References

1 X. Hou, Y. S. Zhang, G. Trujillo-de Santiago, M. M. Alvarez, J. Ribas, S. J. Jonas, P. S. Weiss, A. M. Andrews, J. Aizenberg and A. Khademhosseini, *Nat. Rev. Mater.*, 2017, **2**, 1–15.
2 K. Ren, W. Dai, J. Zhou, J. Su and H. Wu, *Proc. Natl. Acad. Sci. U. S. A.*, 2011, **108**, 8162–8166.
3 S. L. Percival, L. Suleman, C. Vuotto and G. Donelli, *J. Med. Microbiol.*, 2015, **64**, 323–334.
4 J. S. VanEpps and J. G. Younger, *Shock*, 2016, **46**, 597–608.
5 Z. Hazan, J. Zumeris, H. Jacob, H. Raskin, G. Kratysh, M. Vishnia, N. Dror, T. Barliya, M. Mandel and G. Lavie, *Antimicrob. Agents Chemother.*, 2006, **50**, 4144–4152.
6 J. H. Park and Y. H. Bae, *Biomaterials*, 2002, **23**, 1797–1808.
7 V. Lazar, *Anaerobe*, 2011, **17**, 280–285.
8 K. K. Lai and S. A. Fontecchio, *Am. J. Infect. Control*, 2002, **30**, 221–225.
9 J. Lellouche, E. Kahana, S. Elias, A. Gedanken and E. Banin, *Biomaterials*, 2009, **30**, 5969–5978.
10 G. Regev-Shoshani, M. Ko, C. Miller and Y. Av-Gay, *Antimicrob. Agents Chemother.*, 2010, **54**, 273–279.
11 V. B. Damodaran and N. S. Murthy, *Biomater. Res.*, 2016, **20**, 18.

 This journal is © The Royal Society of Chemistry 2021

Published on 20 January 2021. Downloaded by Ulsan National Institute of Science & Technology (UNIST) on 3/7/2023 5:43:09 AM.

12 T. Son, E. Yang, E. Yu, K. H. Oh, M.-W. Moon and H.-Y. Kim, *J. Mech. Sci. Technol.*, 2017, **31**, 5407–5414.
13 J. G. Kim, H. J. Choi, K. C. Park, R. E. Cohen, G. H. McKinley and G. Barbastathis, *Small*, 2014, **10**, 2487–2494.
14 C. Hao, Y. Liu, X. Chen, J. Li, M. Zhang, Y. Zhao and Z. Wang, *Small*, 2016, **12**, 1825–1839.
15 G. D. Bixler, A. Theiss, B. Bhushan and S. C. Lee, *J. Colloid Interface Sci.*, 2014, **419**, 114–133.
16 H.-H. Park, K. Sun, D. Lee, M. Seong, C. Cha and H. E. Jeong, *Cellulose*, 2019, **26**, 8775–8788.
17 E. P. Ivanova, J. Hasan, H. K. Webb, V. K. Truong, G. S. Watson, J. A. Watson, V. A. Baulin, S. Pogodin, J. Y. Wang, M. J. Tobin, C. Löbbe and R. J. Crawford, *Small*, 2012, **8**, 2489–2494.
18 N. MacCallum, C. Howell, P. Kim, D. Sun, R. Friedlander, J. Ranisau, O. Ahanotu, J. J. Lin, A. Vena, B. Hatton, T. S. Wong and J. Aizenberg, *ACS Biomater. Sci. Eng.*, 2015, **1**, 43–51.
19 A. K. Epstein, T. S. Wong, R. A. Belisle, E. M. Boggs and J. Aizenberg, *Proc. Natl. Acad. Sci. U. S. A.*, 2012, **109**, 13182–13187.
20 S. Kim, Y. Jang, L. K. Jang, S. H. Sunwoo, T. I. Kim, S. W. Cho and J. Y. Lee, *J. Mater. Chem. B*, 2017, **5**, 4507–4513.
21 J. C. Tiller, C. J. Liao, K. Lewis and A. M. Klibanov, *Proc. Natl. Acad. Sci. U. S. A.*, 2001, **98**, 5981–5985.
22 G. D. Bixler and B. Bhushan, *Philos. Trans. R. Soc., A*, 2012, **370**, 2381–2417.
23 L. Pocivavsek, J. Pugar, R. O'Dea, S.-H. Ye, W. Wagner, E. Tzeng, S. Velankar and E. Cerda, *Nat. Phys.*, 2018, **14**, 948–953.
24 E. Lee and S. Yang, *MRS Commun.*, 2015, **5**, 97–114.
25 A. E. Tilley, M. S. Walters, R. Shaykhiev and R. G. Crystal, *Annu. Rev. Physiol.*, 2015, **77**, 379–406.
26 H. Zhao, Q. Sun, X. Deng and J. Cui, *Adv. Mater.*, 2018, **30**, 1802141.
27 A. Tovaglieri, A. Sontheimer-Phelps, A. Geirnaert, R. Prantil-Baun, D. M. Camacho, D. B. Chou, S. Jalili-Firoozinezhad, T. de Wouters, M. Kasendra, M. Super, M. J. Cartwright, C. A. Richmond, D. T. Breault, C. Lacroix and D. E. Ingber, *Microbiome*, 2019, **7**, 43.
28 M. E. Johansson, H. Sjövall and G. C. Hansson, *Nat. Rev. Gastroenterol. Hepatol.*, 2013, **10**, 352–361.
29 M. S. H. Boutilier, J. Lee, V. Chambers, V. Venkatesh and R. Karnik, *PLoS One*, 2014, **9**, e89934.
30 T. Kang, X. Banquy, J. Heo, C. Lim, N. A. Lynd, P. Lundberg, D. X. Oh, H. K. Lee, Y. K. Hong, D. S. Hwang, J. H. Waite, J. N. Israelachvili and C. J. Hawker, *ACS Nano*, 2016, **10**, 930–937.
31 C. M. Kirschner and A. B. Brennan, *Annu. Rev. Mater. Res.*, 2012, **42**, 211–229.
32 P. Shivapooja, Q. M. Wang, B. Orihuela, D. Rittschof, G. P. López and X. H. Zhao, *Adv. Mater.*, 2013, **25**, 1430–1434.
33 H. Gu, S. W. Lee, S. L. Buffington, J. H. Henderson and D. C. Ren, *ACS Appl. Mater. Interfaces*, 2016, **8**, 21140–21144.
34 L. Pocivavsek, S. H. Ye, J. Pugar, E. Tzeng, E. Cerda, S. Velankar and W. R. Wagner, *Biomaterials*, 2019, **192**, 226–234.
35 S. Zhang, Y. Wang, P. R. Onck and J. M. J. den Toonder, *Adv. Funct. Mater.*, 2018, **29**, 1806434.
36 P. Shivapooja, Q. Wang, L. M. Szott, B. Orihuela, D. Rittschof, X. Zhao and G. P. López, *Biofouling*, 2015, **31**, 265–274.
37 V. Levering, Q. Wang, P. Shivapooja, X. Zhao and G. P. López, *Adv. Healthcare Mater.*, 2014, **3**, 1588–1596.
38 A. K. Epstein, D. Hong, P. Kim and J. Aizenberg, *New J. Phys.*, 2013, **15**, 095018.
39 H. Geng and S. K. Cho, *Lab Chip*, 2019, **19**, 2275–2283.
40 I. Francolini and G. Donelli, *FEMS Immunol. Med. Microbiol.*, 2010, **59**, 227–238.
41 P. J. Yoo, S. J. Choi, J. H. Kim, D. Suh, S. J. Baek, T. W. Kim and H. H. Lee, *Chem. Mater.*, 2004, **16**, 5000–5005.
42 J. Rychlewski, *J. Appl. Math. Mech.*, 1984, **48**, 303–314.
43 G. Hou, J. Wang and A. Layton, *Commun. Comput. Phys.*, 2012, **12**, 337–377.
44 H. Ko, H.-H. Park, H. Byeon, M. Kang, J. Ryu, H. J. Sung, S. J. Lee and H. E. Jeong, *Sci. Adv.*, 2019, **5**, eaax8935.
45 H.-H. Park, K. Sun, M. Seong, M. Kang, S. Park, S. Hong, H. Jung, J. Jang, J. Kim and H. E. Jeong, *ACS Macro Lett.*, 2018, **8**, 64–69.
46 W. G. Herrick, T. V. Nguyen, M. Sleiman, S. McRae, T. S. Emrick and S. R. Peyton, *Biomacromolecules*, 2013, **14**, 2294–2304.
47 S. Park, H.-H. Park, K. Sun, Y. Gwon, M. Seong, S. Kim, T. E. Park, H. Hyun, Y. H. Choung, J. Kim and H. E. Jeong, *ACS Nano*, 2019, **13**, 11181–11193.
48 S. Chen, L. Li, C. Zhao and J. Zheng, *Polymer*, 2010, **51**, 5283–5293.
49 M. F. Ismail, B. Khorshidi and M. Sadrzadeh, *J. Membr. Sci.*, 2019, **590**, 117270.
50 B. Soltannia, M. A. Islam, J.-Y. Cho, F. Mohammadtabar, R. Wang, V. A. Piunova, Z. Almansoori, M. Rastgar, A. J. Myles, Y.-H. La and M. Sadrzadeh, *J. Membr. Sci.*, 2020, **598**, 117686.
51 N. Yonet-Tanyeri, M. H. Rich, M. Lee, M. H. Lai, J. H. Jeong, R. J. DeVolder and H. Kong, *Biomaterials*, 2013, **34**, 8416–8423.
52 J. Li and W. J. Kao, *Biomacromolecules*, 2003, **4**, 1055–1067.
53 W. G. Bae, H. Ko, J. Y. So, H. Yi, C. H. Lee, D. H. Lee, Y. Ahn, S. H. Lee, K. Lee, J. Jun, H. H. Kim, N. L. Jeon, W. Jung, C. S. Song, T. Kim, Y. C. Kim and H. E. Jeong, *Sci. Transl. Med.*, 2019, **11**, eaaw3329.
54 R. Hartmann, P. K. Singh, P. Pearce, R. Mok, B. Song, F. Diaz-Pascual, J. Dunkel and K. Drescher, *Nat. Phys.*, 2019, **15**, 251–256.
55 R. Rusconi, J. S. Guasto and R. Stocker, *Nat. Phys.*, 2014, **10**, 212–217.